ld_on_CIE_color_space_based_on_first-principles_calculations.pdf

by

Submission date: 14-Apr-2023 10:31AM (UTC+0700)
Submission ID: 2064084051
File name: ld_on_CIE_color_space_based_on_first-principles_calculations.pdf (2.87M)
Word count: 8305
Character count: 42537

Optical Materials: X 16 (2022) 100184

Contents lists available at ScienceDirect

Optical Materials: X

journal homepage: www.journals.elsevier.com/optical-materials-x

Color coordination of emerald on CIE color space based on first-principles calculations

Mega Novita [a,*], Rizky Muliani Dwi Ujianti [a], Fafa Nurdyansyah [a], Slamet Supriyadi [a], Dian Marlina [b], Retno Ambarwati Sigit Lestari [c], Benjamin Walker [d], Nora Izzati Binti Mohd Razip [e], Hironori Kiyooka [e], Shota Takemura [e], Kazuyoshi Ogasawara [e]

[a] Faculty of Engineering and Informatics, Universitas PGRI Semarang, Semarang, 50125, Central Java, Indonesia
[b] Faculty of Pharmacy, Universitas Setia Budi, Surakarta, 57127, Central Java, Indonesia
[c] Faculty of Engineering, Universitas 17 Agustus 1945, Semarang, 50133, Central Java, Indonesia
[d] 925 Dalney Street NW, Atlanta, GA, 30318, USA
[e] School of Science and Technology, Kwansei Gakuin University, Sanda, 669-1337, Hyogo, Japan

ARTICLE INFO

Keywords:
CIE
Emerald
Inactive space
First-principles

ABSTRACT

$Be_3Al_2(SiO_3)_6$ including Cr^{3+} known as emerald have been widely studied and utilized for solid-state laser materials. Numerous theoretical investigations on these systems have also been published in the literature since the electronic energy levels, optical properties, and structures of Cr^{3+} impurities in emerald systems have been thoroughly investigated using a variety of experimental approaches. In general, semi-empirical computations have been used to accomplish the majority of theoretical interpretations of experimental data. Although in the case of non-empirical calculations, the agreement between theoretical and experimental optical properties was improved by taking into account the energy corrections, quantitative evaluation of the color of emitted light was not feasible until recently. Here, the color coordinates of emerald under the standard illuminant has been calculated to perform a quantitative evaluation based on the optical spectra. The "theoretical" color was calculated and presented visually on the Commission Internationale d'Eclairage (CIE) color space based on the theoretical spectra obtained non-empirically using the so-called first-principles discrete variational multi-electron method, known as DVME. The absorption spectra of emerald were calculated using CrO_6^{9-} model cluster with D_3 symmetry. Several key effects in reproducing optical spectra were investigated in detail, such as lattice relaxation, energy correction, and orbital effects. The accuracy of this approach in predicting absorption spectra was analyzed thoroughly under various computational conditions. The results show that accounting for all of the above effects is important to producing the absorption spectra. Specifically, enlarging the considered orbital in the calculation improved the agreement between the computed and experimentally-observed colors. This study is crucial for validating the non-empirical calculations made using the DVME approach to assess the color of emitted light quantitatively.

1. Introduction

The transition between multiplet energy levels of lanthanide, actinide, and transition metal (TM) ions in crystalline and glass system are used by luminescent materials including solid-state lasers and lighting phosphors. Among such luminescent materials, lasers have drawn attention due to their application in the fields of high-speed and high density communication, semiconductor processing, medical applications, etc. In contrast to gas or dye lasers, solid-state lasers have taken on essential roles both scientific and technological fields because of superior output, efficiency, compactness, etc. Examples of Cr^{3+}-doped crystals that have been extensively explored and used for solid-state laser material applications, including ruby (Al_2O_3), alexandrite ($BeAl_2O_4$), and emerald ($Be_3Al_2(SiO_3)_6$). In addition to being a precious stone, emerald has numerous applications an efficient, wide-band, tunable laser gain medium. These materials are well-suited to these applications because of their optical properties, *i.e.* the absorption of visible light originating from the transition between the multiplet energy levels of

* Corresponding author.
E-mail address: novita@upgris.ac.id (M. Novita).

https://doi.org/10.1016/j.omx.2022.100184
Received 31 July 2022; Received in revised form 26 August 2022; Accepted 27 August 2022
Available online 15 September 2022

the impurity states. To achieve R-line emissions, the Cr^{3+} $^4A_2 \rightarrow {}^4T_2$ transitions specifically correlate to excitation and laser pumping [1–4]. The combination of the interaction between the crystal field of the lattice and the electrostatic field of the Cr^{3+} dopant ion, and the presence of electron-phonon coupling, results in tunable solid-state lasing through broadband absorption and emission. Theoretical studies that examine these results have been conducted due to several factors, including electronic energy levels, local characteristics, and structures of the Cr^{3+} impurities in emerald systems have been thoroughly investigated using a variety of experimental approaches [5,6]. Atanasov's group has recently conducted investigations on the electronic structure, energy, and vibronic structure of d-d optical transition [7]. In the context of semi empirical crystal-field theory (CFT) or ligand-field theory (LFT), the majority of studies has been focused on energy levels, ligand-field parameters (LFPs), and spin-Hamiltonian parameters (SHPs) [8–12]. LFT has been effectively used to explain the optical characteristics of TM ions in crystals, as has been described [13]. But because the crystal-field parameter and Racah parameters B and C are used to represent multiplet energies, a number of empirical parameters must be determined from optical spectra based on experimentally observed peaks. The only materials to which it may be used are those for which experimental data are available. On the other hand, great progress has been made in calculating the electronic structure of TM impurities using first-principles analytical methods which utilize density functional theory (DFT). The one-electron approximation, which is the foundation of the majority of general approaches, makes it challenging to estimate absolute multiplet energies in the optical spectrum. In the past, we conducted non-empirical research on the optical characteristics of 3d ions doped in a variety of crystals using the discrete variational multi-electron (DVME) approach [14–26]. This procedure makes use of the configuration interaction (CI) method, which is based on the discrete variational Xα (DV-Xα) molecular orbital (MO) method. There are two versions of the DVME software that were developed by Prof. Ogasawara's group: relativistic and non-relativistic DVME [27,28]. This method is not only effective on a series of crystals doped with transition metal ions, but also rare earth ions [29–32]. Although the CI computation with corrections increased the concordance between theoretically estimated and empirically observed optical parameters, quantitative assessment of the color of the produced light was not previously possible. One of the typical color metrics used to describe emitted light is chromaticity. It is determined by using the absorption spectrum. The Commission Internationale d'Eclairage (CIE) color space is the most widely used model [33,34]. Without relying on empirical values, our most recent study successfully computed the chromaticity coordinates of ruby using the DVME approach [35].

In this study, we use the DVME mehod to perform first-principles calculations on the multiplet structure and absorption spectra of emerald. Analysis was conducted on the accuracy of this method in predicting theoretical characteristics of emerald. Specifically, the effects of lattice relaxation, energy correction, and orbitals on the optical spectra were investigated in detail. The theoretical absorption spectra of emerald were evaluated quantitatively by calculating the chromaticity coordinates (expressed in x and y) under standard illuminants (D65) and compared with their experimental counterparts on the CIE color space chromaticity diagram.

2. Computational procedure

A. Model cluster

Beryl, ($Be_3Al_2(SiO_3)_6$), is a ring silicate mineral. Bragg and West published the first study on beryl's hexagonal structure with $P6/mcc$ space group in 1927 [36]. Beryl, commonly known as goshenite, is a solid that clear and colorless in its pure state [37] because of its large band gap, which permits the passage of visible light [37]. When transition-metal dopants like Fe, Mn, V, and Cr are added to beryl's crystal structure, a range of beryl variations are produced. These dopants serve as chromophores and change the color of the host [38–40]. For instance, the color emerald is produced when Cr^{3+} (and occasionally V^{3+}) ions are replaced at Al^{3+} sites (green beryl) [41]. Beryl's aquamarine color is derived from the ion Fe^{2+}, while its gold-yellow hue, often known as gold beryl (or heliodor), is derived from the ion Fe^{3+} [42–44]. Mn^{2+} ions produce the pink or rose-colored mineral morganite, whereas Mn^{3+} ions produce the red mineral bixbite [45,46].

The lattice constants of the beryl's unit cell are $a = 9.209$ and $c = 9.197$ Å [36]. Based on the beryl crystal, a model cluster with seven D_3-symmetric atoms was created. At the core of the CrO_6^{9-} model cluster was the impurity Cr^{3+}. Fig. 1 shows the beryl crystal structure and the constructed model cluster which were drawn by VESTA [47]. A Madelung potential was constructed by adding thousands of point charges to external atomic sites. Here, +3 for Al and −2 for O. They were chosen to ensure charge neutrality by having a combined charge of zero for the model cluster and the point charges. It consisted of 216,000 sample sites. We next used the extended X-ray absorption fine structure (EXAFS) data of emerald performed by Gaudry et al. [48] to investigate how lattice relaxation influences the electronic structure around Cr^{3+} ion in $Be_3Al_2(SiO_3)_6$. The Cr–O distance in $Be_3Al_2(SiO_3)_6$: Cr^{3+} was observed to be 1.975 Å, which is 103.06% larger than the Al–O distance in pure $Be_3Al_2(SiO_3)_6$. In most minerals, Cr^{3+} ions may replace Al^{3+} ions and operate as luminous or laser-active centers because they are stabilized by six-fold coordination environments. Cr^{3+} ionic's radius (0.615 Å) is significantly larger than Al^{3+} (0.535 Å) [49,50], therefore this substitution may have an impact on the crystalline lattice's shape in addition to the color.

B. Theoretical absorption spectra

In this study, we use the discrete variational multi-electron method to determine the theoretical absorption spectra of emerald without using empirical data (DVME). This method is a combination between the one-electron approach known as discrete variational Xα (DV-Xα) method and the many-electron configuration interaction (CI) method. There are two steps in the DVME procedure. The DV-X approach is used in the first stage to calculate one-electron molecular orbitals (MOs) [51]. As basis functions, atomic orbitals (AO) produced numerically are employed [51]. The self-consistent-field computation optimizes the AOs for the chemical environment.

In theory, the computation of systems with nuclei and electrons in quantum mechanics yields the electronic structures of materials. The Schrödinger equation gives the following expression for a molecule's electronic structure:

$$h\psi(\mathbf{r}) = \varepsilon\psi(\mathbf{r}) \tag{1}$$

where $\mathbf{r}$ is the position of a given electron, whereas ψ and ε are the MO

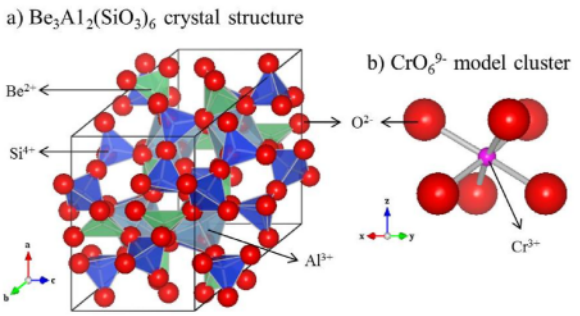

Fig. 1. The crystal structure of (a) $Be_3Al_2(SiO_3)_6$ and (b) CrO_6^{9-} model cluster from the calculations. They were drawn by VESTA [47].

wave function and energy of the system, respectively. The one-electron Hamiltonian, denoted by h in this instance, is given by

$$h(\mathbf{r}) = \frac{1}{2}\nabla^2 + V(\mathbf{r}). \tag{2}$$

where the effective molecular potential $V(\mathbf{r})$ is given by:

$$V(\mathbf{r}) = -\sum_v \frac{Z_v}{|\mathbf{r}-\mathbf{R}_v|} + \int \frac{\rho(\mathbf{r}')}{|\mathbf{r}'-\mathbf{r}|}d\mathbf{r}' - 3\alpha\left\{\frac{3}{8\pi}\rho(\mathbf{r})\right\}^{1/3}, \tag{3}$$

where Z_v and $\mathbf{R}_v$ are, the atomic number and position of atom v, respectively. The nuclear attraction potential and the repulsive potential of the system's electron cloud are, respectively, the first two components of Eq. (3). The exchange-correlation potential suggested by Slater [52] is the third term. Since research has indicated that this is the most suitable value for most occurrence, α was set to 0.7 [53]. The density of electron, ρ, is determined by

$$\rho(\mathbf{r}) = \sum_l \rho_l(\mathbf{r}) = \sum_l f_l|\varphi_l(\mathbf{r})|^2 \tag{4}$$

where f_l is the occupancy of φ_l.

The electric dipole transition-related oscillator strength is computed by

$$I_{if} = 2\left(E_f - E_i\right)\left|\psi_f\left|\mathbf{r}\cdot\mathbf{e}\right|\psi_i\right|^2 \tag{5}$$

or

$$I_{if} = \frac{2}{3}\left(E_f - E_i\right)\left|\psi_f\left|\mathbf{r}\right|\psi_i\right|^2, \tag{6}$$

for either anisotropic or average calculations, respectively. The one-electron wave functions for the initial and final states are expressed by ψ_i and ψ_f , respectively.

The key portion of the DVME approach is the second stage, where the many-electron computations utilizing the CI method are carried out. The electron-electron interactions in this scenario are computed directly. The many-electron Schrödinger equation is given by:

$$\boldsymbol{H\Psi} = \boldsymbol{E\Psi} \tag{7}$$

where E and Ψ are the energy of the system and the many-electron wave function, respectively. Ψ is given by:

$$\boldsymbol{\Psi}_l = \sum_{j=1}^{n} W_{jl}\boldsymbol{\Phi}_j \tag{8}$$

where, accordingly, n is the total number of Slater determinants which form a linear combination used in the CI calculation, and W_{jl} is the coefficient of the jth Slater determinant in the lth many-electron wave function. $\boldsymbol{\Phi}_j$ is given by:

$$\boldsymbol{\Phi}_j\left(\mathbf{r}_1, \ldots, \mathbf{r}_n\right) = \frac{1}{\sqrt{n!}}\begin{vmatrix} \varphi_{j1}(\mathbf{r}_1) & \varphi_{j1}(\mathbf{r}_2) & \cdots & \varphi_{j1}(\mathbf{r}_n) \\ \varphi_{j2}(\mathbf{r}_1) & \varphi_{j2}(\mathbf{r}_2) & \cdots & \varphi_{j2}(\mathbf{r}_n) \\ \vdots & \vdots & \ddots & \vdots \\ \varphi_{jn}(\mathbf{r}_1) & \varphi_{jn}(\mathbf{r}_2) & \cdots & \varphi_{jn}(\mathbf{r}_n) \end{vmatrix}, \tag{9}$$

where TM 3d orbitals make up the majority of the molecular orbitals φ_j . H is the many-electron Hamiltonian

$$H = \sum_{i=1}^{M} h(\mathbf{r}_i) + \sum_i \sum_{j>1} g\left(\mathbf{r}_i, \mathbf{r}_j\right), \tag{10}$$

where M is the number of the explicitly-treated electrons, while the one-electron and two-electron operators, h and g, respecively, are given as

$$\begin{cases} h(\mathbf{r}_i) = -\frac{1}{2}\nabla_i^2 + V_{nuc}(\mathbf{r}_i) + V_0(\mathbf{r}_i) \\ g\left(\mathbf{r}_i, \mathbf{r}_j\right) = \frac{1}{r_{ij}} \end{cases}. \tag{11}$$

where $\mathbf{r}_i$ is the location of the ith electron, r_{ij} is the distance between the ith and the jth electrons, V_{nuc} is the nuclear poential, and V_0 is the potential due to all other electrons. As a result, the electrons occupies the impurity levels are given explicit treatment. H is diagonalized within the subspace spanned by the Slater determinants Φ_i that are created from the impurity-state orbitals acquired from the one-electron MO calculation, resulting in the many-electron wave function and multiplet energies. Each matrix element of the effective many-electron Hamiltonian H between two Slater determinants, Φ_p and Φ_q, is given by:

$$H_{pq} = \Phi_p\left|H\right|\Phi_q = \sum_{i=1}^{L}\sum_{j=1}^{L} A_{ij}^{pq}\left\langle i\right|\left|h\right|\left|j\right\rangle + \sum_{i=1}^{L}\sum_{j=1}^{L}\sum_{k=1}^{L}\sum_{l=1}^{L} B_{ijkl}^{pq}\left\langle ij\right|\left|g\right|\left|kl\right\rangle. \tag{12}$$

A_{ij}^{pq} and B_{ijkl}^{pq} are coefficients produced by the expanding Slater determinants, where L is the number of impurity-state orbitals. The definitions of $\langle i|h|j\rangle$ and $\langle ij|g|kl\rangle$ are

$$\left\langle i\right|\left|h\right|\left|j\right\rangle = \int \varphi_i^*(\mathbf{r})h(\mathbf{r})\varphi_j(\mathbf{r})d\mathbf{r} \tag{13}$$

and

$$\left\langle ij\right|\left|g\right|\left|kl\right\rangle = \int\int \varphi_i^*(\mathbf{r}_1)\varphi_j^*(\mathbf{r}_2)\frac{1}{r_{12}}\varphi_k(\mathbf{r}_1)\varphi_l(\mathbf{r}_2)d\mathbf{r}_1 d\mathbf{r}_2, \tag{14}$$

φ stands for the chosen orbitals determined by the cluster calculation. The following equations are used to numerically compute these matrix elements using the DV integration technique [54]:

$$\left\langle i\right|\left|h\right|\left|j\right\rangle = \sum_\alpha \omega(\mathbf{r}_\alpha)\varphi_\alpha^*(\mathbf{r}_\alpha)h(\mathbf{r}_\alpha)\varphi_j(\mathbf{r}_\alpha) \tag{15}$$

and

$$\left\langle ij\right|\left|g\right|\left|kl\right\rangle = \sum_\alpha \omega(\mathbf{r}_\alpha)\varphi_i^*(\mathbf{r}_\alpha)\left[\sum_{\beta(\neq\alpha)} \omega\left(\mathbf{r}_\beta\right)\varphi_i^*\left(\mathbf{r}_\beta\right)\frac{1}{\mathbf{r}_{\alpha\beta}}\varphi_l\left(\mathbf{r}_\beta\right)\right]\varphi_k(\mathbf{r}_\alpha). \tag{16}$$

here, $\mathbf{r}_\alpha$ is a sampling point and ω is a weighting function that is proportional to the inverse of the sampling point density. The Hamiltonian matrix is diagonalized to get the multiplet energy levels.

In the second stage, the many-electron wave functions which correspond to each multiplet state may be created by linearly combining the Slater determinants and the eigenvector produced from diagonalizing the many-electron Hamiltonian. Consequently, the oscillator strength for the electric-dipole transition between multiplets (transition probability) is computed by

$$I_{if} = 2\left(E_f - E_i\right)\left|\Psi_f\left|\sum_{k=1}^{n}\mathbf{r}_k\cdot\mathbf{e}\right|\Psi_i\right|^2 \tag{17}$$

or

$$I_{if} = \frac{2}{3}\left(E_f - E_i\right)\left|\Psi_f\left|\sum_{k=1}^{n}\mathbf{r}_k\right|\Psi_i\right|^2, \tag{18}$$

for either anisotropic and average calculations, respectively, are the many-electron wave functions of the initial and final states' and are denoted by Ψ_i and Ψ_f, respectively. Their respective energy eigenvalues are E_i and E_f. The unit vector $\mathbf{e}$ is parallel to the electric field of the incoming light, and $\mathbf{r}$ is the location of the electron. In this work, calculations based on 3 d^3 configuration and on 3 d^3 and inactive $2p^{36}$

orbitals originating from oxygen are introduced. Typically, ${}_{10}C_3 = 120$ Slater determinants built with 10MOs mostly composed of TM 3d orbitals were utilized as basis functions in the investigation of TM 3 d^3-doped crystals utilizing the DVME approach. However, we present a strategy to take into account inactive oxygen 2p orbitals in the CI calculation used for the linear combination in order to increase the agreement with the experiment. As a result, we obtained ${}_{36}C_{36} + {}_{10}C_3 = 121$ Slater determinants. It was built using the 46 MOs which were made up of 10MOs of transition metal 3d orbitals, and 36 MOs of inactive 2p orbitals. They were used as the basis functions.

C. Energy Correction

Numerous-electron CI computations often overestimate multiplet energies by around 20% due to overestimation of crystal field splitting [27]. However, using Slater's transition-state calculations, one-electron MO computations may determine the energy difference between various configurations [52]. As a result, the computation applies a correction to the barycenter of each configuration based on the one-electron MO calculation, known as the configuration dependent correction (CDC). The barycenters of the configurations $(t_{2g})^3$, $(t_{2g})^2(e_g)^1$, $(t_{2g})^1(e_g)^2$, and $(e_g)^3$ were changed to be 0, $10Dq$, $20Dq$, and $30Dq$, respectively. In this case, the value of $10Dq$ was derived from the one-electron MO calculation in the previous step. This method uses the Hamiltonian as

$$H_{pq}^{CDC} = H_{pq} + D_{CDC}(m,n)\delta_{pq} \tag{19}$$

The correction to the terms corresponding to the $t_{2g}^m e_g^n$ configuration is $D_{CDC}(m,n)\mathrm{D_{CDC}(m,n)}$, and δ_{pq} is defined as

$$\delta_{pq} = \begin{cases} 1\ for\ (p = q) \\ 0\ for\ (p \neq q) \end{cases}. \tag{20}$$

The energy gap between adjacent configurations $(t_{2g})^m(e_g)^n$ and $(t_{2g})^{m-1}(e_g)^{n+1}$ may be properly represented by the one-electron energy difference, $\Delta(m,n;m-1,n+1) = \varepsilon_{eg} - \varepsilon_{t2g}$, and in the term of Slater's transition state, $(t_{2g})^{m-0.5}(e_g)^{n+0.5}$, according to the Slater's transition state method [52]. Consequently, the relation may be used to find the value of $D_{CDC}\ (m,n)$ as

$$\frac{1}{N(m,n)} \sum_{(m^p,\ n^p)=(m,n)} H_{pp}^{CDC} - \frac{1}{N(m-1,n+1)} \sum_{(m^p,\ n^p)=(m-1,n+1)} H_{pp}^{CDC} = \Delta(m,n;m-1,n+1) \tag{21}$$

where $N(m,n)$ is the number of Slater determinants that corresponds to the $(t_{2g})^m(e_g)^n$ configuration. m^p and n^p are the numbers of electrons occupying the t_{2g} and e_g states in the pth Salter determinant, respectively. The configuration (m,n) has little impact on the value of $\Delta(m,n,m-1,n+1)$. As a result, $\Delta(m,n,m-1,n+1)$ for all configurations is roughly acquired form the value derived in the ground state:

$$\Delta(m,n,m-1,n+1) = e_g^{GS} - t_{2g}^{GS} = \Delta_{eff} \tag{22}$$

It is expressed as

$$\frac{1}{N(m,n)} \sum_{(m^p,\ n^p)=(m,n)} H_{pp}^{CDC} = n\Delta_{eff} \tag{23}$$

Because of the small number of Slater determinants, the effects of electron correlation are overstated by around 10–50%, whereas the electron-electron repulsion integrals are underestimated [55]. The number of Slater determinants can be gradually increased, although doing so is computationally costly. Therefore, applying the correlation correction (CC) to account for the residual influence of electron correlation is a more effective method for quantitatively estimating the absolute multiplet energies. In this method, a correlation factor c (correlation correction factor) is multiplied by each matrix element of the electron-electron repulsion operator. The c factor was obtained from first-principle calculations based on consistency among the spin-flip transition energy, from $(t_{2g}\uparrow)^3$ to $(t_{2g}\uparrow)^2(t_{2g}\downarrow)^1$. It is between the many electron CI calculations and the spin-polarized one-electron MO calculations.

By multiplying the correction factor c by the Coulombic electron-electron repulsion operator $1/r_{ij}$ in Eq. (11) (thereby becoming c/r_{ij}). CC is a technique for more precisely approximating the underestimated electron correlation effect. The consistency between the spin-polarized MO and the multiplet calculations, as will be discussed later, may be used to derive the correction factor c (CC factor) without using any empirical data. The spin-flip transition energy ε^{SF} from $(t_{2g}\uparrow)^3$ and $(t_{2g}\uparrow)^2(t_{2g}\downarrow)^1$ configurations using Slater's transition state method as follows,

$$\varepsilon^{SF} = \varepsilon_{t\downarrow}^{TS} - \varepsilon_{t\uparrow}^{TS} \tag{24}$$

Both $\varepsilon_{t\downarrow}^{TS}$ and $\varepsilon_{t\uparrow}^{TS}$ are the energies of $t_{2g}\uparrow$ and $t_{2g}\downarrow$ orbitals in the $(t_{2g}\uparrow)^{2.5}(t_{2g}\downarrow)^{0.5}$ configuration, respectively.

The four distinct states, ${}^2T_{2g}$, ${}^2T_{1g}$, ${}^2E_g$, ${}^4A_{2g}$ ($S_z = 1/2$) are represented by the $(t_{2g}\uparrow)^2(t_{2g}\downarrow)^1$ configuration S_z represents the z-component of the total spin. Therefore, the average transition energy is expressed by:

$$\varepsilon^{SF}(c) = \frac{\sum_k g_k E_k(c)}{\sum_k g_k}, \tag{25}$$

were g_k denotes the final state's degeneracy in the kth order. For ${}^2T_{2g}$, ${}^2T_{1g}$, ${}^2E_g$, ${}^4A_{2g}$ ($S_z = 1/2$), the actual values of g_k are 3, 3, 2, and 1, respectively. The spin-flip transition energy and multiplet energies rely on the CC factor c since it is used in the Hamiltonian of the multiplet calculation. The following relation may be used to establish the CC factor c since $\varepsilon^{SF}(c)$ should be equal to the spin-flip transition energy obtained from the one-electron calculation.

$$\varepsilon^{SF}(c) = \varepsilon_{t\downarrow}^{TS} - \varepsilon_{t\uparrow}^{TS}. \tag{26}$$

In the actual computation, it is not easy to arrive at an analytical solution to Eq. (24). Hence, $\varepsilon^{SF}(c)$ was repeatedly computed while progressively increasing the c's value until Eq. (24) is fulfilled within an error of 10^{-5} Hartree. In the CDC-CC approach which considers both CDC and CC, the final effective Hamiltonian is written as,

$$\Phi_p \left| H^{CDC-CC} \right| \Phi_q = \sum_{i=1}^{L}\sum_{j=1}^{L} A_{ij}^{pq} \left| i \right| h \left| j \right| + \sum_{i=1}^{L}\sum_{j=1}^{L}\sum_{k=1}^{L}\sum_{l=1}^{L} c \times B_{ijkl}^{pq} \left| ij \right| g \left| kl \right| + D_{CDC}(m,n)\delta_{pq} \tag{27}$$

D. CIE color coordination

Using the CIE 1931 chromaticity diagram, we assess the color parameters. x and y graph coordinates are used to depict the color of the light that is being emitted. Red, green, and blue color ratios are used to represent this graph. The tristimulus values X, Y, Z are three colors that represent the band-pass filtered chromaticity response of cones in the human retina. The transmittance, which is determined from absorbance, was used as the basis for calculating the chromaticity coordinates. The definition of transmittance is

$$T(\lambda) = \frac{I(\lambda)}{I_0(\lambda)} \tag{28}$$

where I_0 and I stand for incident and transmitted light intensities, respectively. On the other hand, the definition absorbance is

$$A(\lambda) = -\log\left(\frac{I(\lambda)}{I_0(\lambda)}\right) \tag{29}$$

Consequently, the transmittance is determined by

$$T(\lambda) = e^{-A(\lambda)} \tag{30}$$

Next, X, Y, and Z are written as

$$\begin{aligned} X &= \int_{380}^{780} T(\lambda)P(\lambda)\bar{x}(\lambda)d\lambda = \int_{380}^{780} e^{-A(\lambda)}P(\lambda)\bar{x}(\lambda)d\lambda \\ Y &= \int_{380}^{780} T(\lambda)P(\lambda)\bar{y}(\lambda)d\lambda = \int_{380}^{780} e^{-A(\lambda)}P(\lambda)\bar{y}(\lambda)d\lambda \\ Z &= \int_{380}^{780} T(\lambda)P(\lambda)\bar{z}(\lambda)d\lambda = \int_{380}^{780} e^{-A(\lambda)}P(\lambda)\bar{z}(\lambda)d\lambda \end{aligned} \tag{31}$$

Standard illuminant D65, or daylight, is denoted by the symbol $P(\lambda)$. In general, the coefficient of molar absorption ε, the molar concentration of particles (Cr^{3+} in this case) c, and the sample's thickness l all influence absorbance.

$$A(\lambda) = \varepsilon(\lambda)cl \tag{32}$$

Since $c_2l_2 = ac_1l_1$ must be fulfilled, the product of absorbance and a scalar, such as $A_2 = aA_1(\lambda)$, indicates that either the sample's concentration and/or the sample's thickness have been altered. The chromaticity coordinates (x, y) are then calculated as

$$\begin{aligned} x &= \frac{X}{X+Y+Z} \\ y &= \frac{Y}{X+Y+Z} \end{aligned} \tag{33}$$

3. Results and discussion

A. Molecular orbital energy

Using non-relaxed and relaxed model clusters, the molecular orbital energies of $Be_3Al_2(SiO_3)_6$: Cr^{3+} have been determined and are displayed in Fig. 2. The impurity levels' lowest point is 0. The valence band (VB), which is mostly made up of O 2p orbitals, is shown by black solid lines. The conduction band (CB), which mostly consists of Cr 4s and 4p orbitals, is represented by the black dashed lines. A blue dashed line and a red solid line, respectively, represent the impurity states that split into e_g and t_{2g}.The crystal field splittings estimated from the energy difference between e_g and t_{2g} ($10Dq$) are found to be 1.98 and 1.74 eV for the calculations using nonrelaxed and relaxed model clusters, respectively. Due to the trigonal crystal field's existence, the t_{2g} orbital further divides into the a and e levels. In both circumstances, the $t_{2g}(e)$ energy level is marginally more than that of the $t_{2g}(a)$ level. These splittings were found to be 0.21 and 0.19 eV for the calculations using nonrelaxed and relaxed model clusters, respectively.

B. Absorption spectra analysis

In comparison to alexandrite, topaz, and ruby, emerald has a more complex crystal structure and a weaker crystal field. The location of the U band serves as a quantitative indicator of this [56–58]. The three permitted transitions from the $^4A_{2g}$ ground state to the excited states of $^4T_{2g}$ (4F) (known as U-band), $^4T_{1ga}$ (4F) (known as Y-band), and $^4T_{1gb}$ (4P) (known as Y′-band) are therefore moved to lower energies [59,60]. Since the $2E_g$ state almost independent from the crystal-field strength parameter, $10Dq$, the emission energies resulting from the $^2E_g \rightarrow {}^4A_{2g}$ transition are shown by narrow lines and basically unchanged in their energies [61].

Theoretical $Be_3Al_2(SiO_3)_6$: Cr^{3+} absorption spectra are depicted in Fig. 3 and were estimated using the first-principles DVME approach without the use of empirical parameters. Comparisons are made between theoretical absorption spectra calculated under various

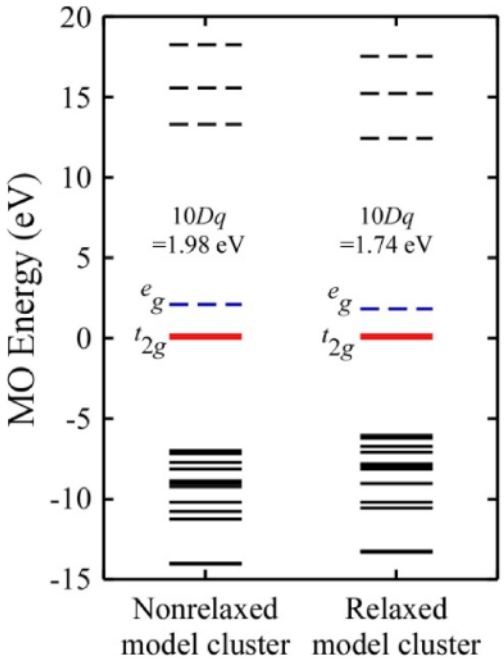

Fig. 2. Molecular orbital (MO) energy (eV) of $Be_3Al_2(SiO_3)_6$: Cr^{3+} calculated based on nonrelaxed and relaxed model clusters. The bottom of the impurity levels are adjusted to zero. The valence band (V), which mostly comprises of O 2p orbitals, is shown by black solid lines. The conduction band, which mostly consists of Cr 4s and 4p orbitals, is represented by the black dashed lines. The blue dashed line and red solid lines, respectively, show the impurity states that split into e_g and t_{2g}. Although relatively small, the t_{2g} orbital splits further into a and e levels. (For interpretation of the references to color in this figure legend, the reader is referred to the Web version of this article.)

computational scenarios including the effects of lattice-relaxation and the energy-correction. On the left panel of Fig. 3a, the spectra that were determined by calculations using 3d orbitals are displayed. The right panel of Fig. 3b displays the spectra that were calculated using the 3d orbital and the inactive 2p orbital. Two peaks emerged from the transition energies from the $^4A_{2g}$ ground state to the $^4T_{2g}$ (U-band) and $^4T_{1ga}$ states (Y-band) in the theoretical absorption spectra calculated using the 3d orbital model. Although they are scarcely perceptible, Y-band energies have far lower intensities than U-band energies. Only the Y-band energy determined by combining the DVME approach with the lattice-relaxation effect stands out. The transition energies from the $^4A_{2g}$ ground state to the $^4T_{2g}$, $^4T_{1ga}$, and $^4T_{1gb}$ states for the first, second, and third peaks, respectively, resulted in three peaks in the calculations based on the 3d orbital and the inactive 2p orbital. The energy of these peaks are commonly referred to as U-, Y-, and Y′ bands, respectively. Nevertheless, the computational condition affects where these peaks are located. The experimental absorption spectra of $Be_3Al_2(SiO_3)_6$: Cr^{3+} were obtained from work reported by Fairbank's group [6] and shown in the bottom of Fig. 3. The transition between the Cr^{3+} ions' ground $^4A_{2g}$ state and excited states, $^4T_{2g}$ and $^4T_{1g}$, results in two large absorption bands in the spectrum. These bands' maxima are located at around 1.99–2.00 eV and 2.85 eV [62], respectively, whereas they are centered at approximately 2.23 eV and 3.04 eV in ruby [63,64]. Evidently, compared to ruby, both of emerald's absorption bands experience a red shift. It is clear from the absorption spectra that the initial absorption band in ruby is at ~2.23 eV (green region), whereas in emerald, it is at ~1.99 eV (red region). These crystals will appear as red and green, respectively, in transmitted light, in accordance with the

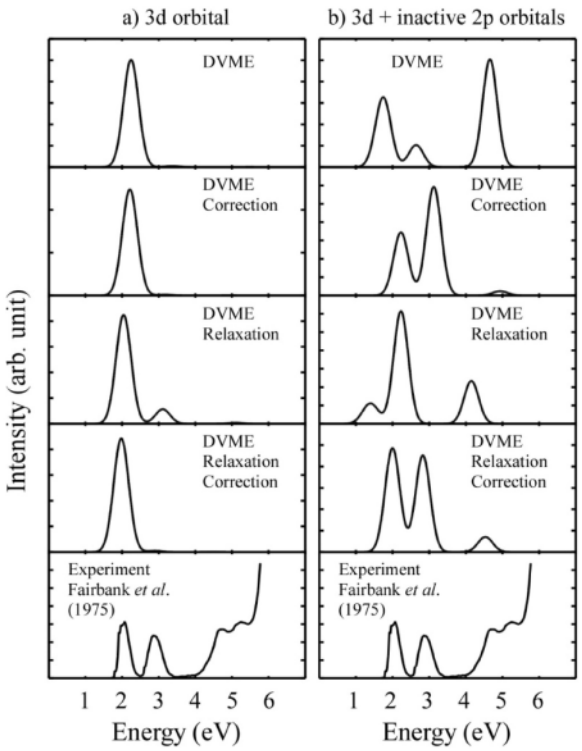

Fig. 3. The $Be_3Al_2(SiO_3)_6$: Cr^{3+} absorption spectra estimated using (a) the 3d orbital alone and (b) the 3d orbital paired with the inactive 2p orbital. Both lattice-relaxation and CDC-CC correction effects were taken into account. The measured absorption spectra from Fairbank et al.'s work may be found at the bottom [6].

complementary color theory. Surprisingly, both materials' R-lines in the emission spectra (which represent the $^2E_g \rightarrow {}^4A_{2g}$ emission transition) are essentially in the same spectral area (ranging from 1.81 to 1.80 eV) [62,63].

Table 1 shows the peak locations of the theoretical absorption spectra presented in Fig. 3. Comparisons are made between the U-, Y-, and Y′-band peaks, which are located at 2.07, 2.86, and 4.74 eV, respectively. The effects of lattice-relaxation effect and the effects of CDC-CC energy adjustment decreased the energies of U- and Y-bands in the calculations that solely used the 3d orbital. The lattice-relaxation effect decreased the energies of U-, Y-, and Y′ band in calculations based on 3d orbitals paired with inactive 2p orbitals. The CDC-CC energy adjustment, however, made those energies stronger. It is clear that enhancing the agreement with the experiment depends significantly on the effects of lattice-relaxation and CDC-CC energy correction. The CC factor (c) in Table 1 indicates that the multiplet splittings were decreased in all cases by about 20%.

Table 2 displays the multiplet energies of $Be_3Al_2(SiO_3)_6$: Cr^{3+} that were computed using the DVME technique under various computational settings, together with the matching experimental results provided by Fairbank's group [6]. Simply only the average energies of each multiplet states are displayed since the splitting caused by the trigonal field is quite minor. As relaxation or energy correction is used, the multiplet energies for every calculation decrease. Both CDC-CC and relaxation lower the multiplet energies in the computation of samples that only take into account the third orbital. For doublet states, the impact of energy correction is greater, but for quartet states, the impact of relaxation is greater. The formulas CDC-CC result in a drop in doublet energy

Table 1
The peak position (eV) of the theoretical absorption spectra of $Be_3Al_2(SiO_3)_6$: Cr^{3+} obtained from the calculations based on the 3d orbital alone and the 3d orbital paired with the inactive 2p orbital. The CC factors (*c*) are also shown. The experimental peak positions of $Be_3Al_2(SiO_3)_6$: Cr^{3+} were obtained from the measured absorption spectra published by Fairbank et al. [6].

Computational condition		*c*	1st	2nd	3rd
Experiment			2.07	2.86	4.74
3d orbital	DVME	–	2.24	3.37	–
	DVME + correction	0.82	2.21	3.17	–
	DVME + relaxation	–	2.04	3.11	–
	DVME + relaxation + correction	0.84	1.98	2.89	–
3d + inactive 2p orbitals	DVME	–	1.74	2.64	4.64
	DVME + correction	0.81	2.23	3.12	4.94
	DVME + relaxation	–	1.40	2.23	4.15
	DVME + relaxation + correction	0.84	2.00	2.83	4.53

Table 2
The multiplet energies (eV) of $Be_3Al_2(SiO_3)_6$: Cr^{3+} obtained from the calculations based on 3d orbital only and 3d orbital combined with inactive 2p orbital. The CC factors (*c*) are also shown. The experimental transition energies were obtained from literature reported by Fairbank et al. [6].

Computational condition		c	^2E	$^2T_1$	$^2T_2$	$^4T_2$	$^4T_{1a}$
Experiment			1.82			1.99	
3d orbital	DVME		2.40	2.55	3.56	2.27	3.41
	DVME + correction	0.82	1.97	2.10	3.00	2.23	3.19
	DVME + relaxation		2.37	2.52	3.48	2.06	3.16
	DVME + relaxation + correction	0.84	1.98	2.11	2.97	2.00	2.91
3d + inactive 2p orbitals	DVME		2.35	2.52	3.40	1.72	2.74
	DVME + correction	0.81	1.95	2.07	2.98	2.23	3.19
	DVME + relaxation		2.31	2.48	3.23	1.42	2.32
	DVME + relaxation + correction	0.84	1.99	2.11	2.98	1.99	2.90

but an increase in quartet energies when samples with the 3d orbital paired with the inactive 2p orbital are taken into account. Both the doublet and quartet energy drop due to lattice relaxation. Furthermore, all of the multiplet energy are reduced by the greater orbital consideration. The computation using DVME allowing for lattice relaxation revealed a significant effect. According to our calculations, the multiplet energies of the 3d orbital paired with the inactive 2p orbital, taking into consideration the effects of lattice relaxation and energy corrections, show a good agreement with the observed findings.

C. Color coordinate of emerald

In CIE 1931 color space, the chromaticity coordinates (*x*, *y*) of $Be_3Al_2(SiO_3)_6$: Cr^{3+} under the reference illuminant D65 are calculated using (a) the 3d orbital alone and (b) the 3d orbital paired with the inactive 2p orbital (see Fig. 4). They were contrasted under various computational settings that took into consideration the effect of lattice-relaxation and CDC-CC correction. The opened circle (○) shows the color coordinates of the experimental absorption spectra acquired from the research published by Fairbank et al. [56]. Since factors like Cr^{3+} concentration and sample thickness affect color, many points representing various densities were computed and graphically shown.

As concentration grew, the theoretical color coordinates obtained from the calculations utilizing just the 3d orbital moved toward the blue area. Similar to this, based on 3d orbital paired with inactive 2p orbital,

Table 3
CIE chromaticity color coordinate (x, y) of the theoretical color of $Be_3Al_2(SiO_3)_6$: Cr^{3+}. Based on the experimental absorption spectra obtained from Ref. [6], the experimental color coordinates were determined.

Point			1st	2nd	3rd	4th	5th	6th	7th
Experiment		x	0.20	0.14	0.11	0.09			
		y	0.40	0.45	0.48	0.50			
3d orbital	DVME	x	0.31	0.29	0.26	0.22	0.19		
		y	0.33	0.27	0.18	0.11	0.05		
	DVME + correction	x	0.31	0.29	0.26	0.21	0.17		
		y	0.33	0.28	0.22	0.11	0.05		
	DVME + relaxation	x	0.31	0.27	0.24	0.18	0.14	0.14	0.13
		y	0.33	0.30	0.27	0.20	0.13	0.10	0.08
	DVME + relaxation + correction	x	0.31	0.27	0.24	0.24	0.18	0.14	
		y	0.33	0.31	0.28	0.28	0.22	0.16	
3d + inactive 2p orbitals	DVME	x	0.31	0.29	0.28	0.27	0.27	0.27	
		y	0.33	0.35	0.38	0.43	0.46	0.48	
	DVME + correction	x	0.31	0.30	0.29	0.25	0.23		
		y	0.33	0.29	0.26	0.17	0.12		
	DVME + relaxation	x	0.31	0.26	0.22	0.17	0.16		
		y	0.33	0.20	0.12	0.04	0.02		
	DVME + relaxation + correction	x	0.31	0.30	0.28	0.24	0.15	0.10	0.08
		y	0.33	0.35	0.38	0.44	0.58	0.68	0.71

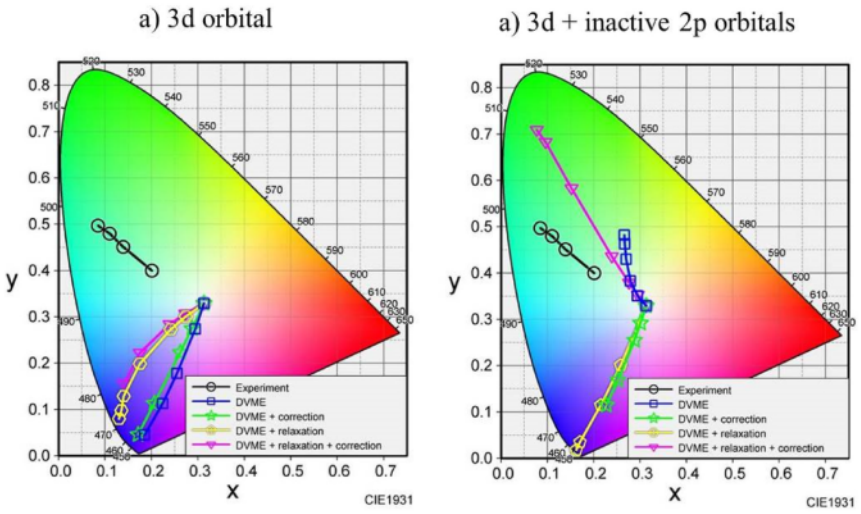

Fig. 4. Color coordination of $Be_3Al_2(SiO_3)_6$: Cr^{3+} in CIE 1931 based on the (a) 3d orbital alone and (b) 3d orbital paired with inactive 2p orbital. The effects of CDC-CC correction and lattice relaxation were taken into consideration in computational settings. The color coordinates of the experimental absorption spectrum obtained from the work reported by Fairbank et al. are shown by opened black circle (○). (For interpretation of the references to color in this figure legend, the reader is referred to the Web version of this article.)

the theoretical color coordinates determined using either DVME + correction and DVME + relaxation went in the same direction. Surprisingly, with simple DVME calculations, the theoretical color coordinates shifted to the green region. When we combined the DVME with relaxation and correction, the results were much closer to the observed data. These techniques effectively mimic the color of emerald since the experimental color coordinates are in the green region. As is evident, the calculations based on the combination of 3d orbital and inactive 2p orbital with DVME method which considers relaxation and energy correction suggest good agreement with the experiment. (see Table 3).

4. Conclusion

Using the DVME approach, the chromaticity coordinates of emerald under the common illumination D65 have been determined non-empirically. In order to construct the theoretical absorption spectra, the many-electron CI calculations were calculated by performing one-electron MO calculations in the first step. The effect of lattice-relaxation and energy correction (CDC-CC) were taken into consideration to increase computation precision. In this study, EXAFS data were used to determine the effect of lattice-relaxation. According to the consistency of the one-electron and many-electron methods, the CDC-CC energy adjustment was calculated in a non-empirical manner. The theoretical absorption spectra for calculations based only on the 3d orbital include two peaks in the visible area coming from the U- and Y-bands. In the calculations which are based on 3d orbital and inactive 2p orbital, the theoretical absorption spectra produced three peaks in the visible region originating from U-, Y-, and Y′-bands. The calculations based on the 3d orbital paired with inactive 2p orbital combined with the effects of lattice-relaxation and energy correction demonstrate good agreement with the measured absorption spectra published by Fairbank et al. [56], among computations with different computing circumstances. Next, the theoretical spectra were used to calculate the CIE chromaticity coordinates by adopting the standard procedures. The findings imply that an important component in identifying the color coordinate of emerald in the CIE color space is the repeatability of theoretical absorption spectra. In this case, good agreement between theoretical and experimental colors was mainly due to the consideration of inactive 2p orbital in the CI calculations.

CRediT authorship contribution statement

Mega Novita: Conceptualization, Methodology, Writing – original draft, Writing – review & editing, Draft. **Rizky Muliani Dwi Ujianti:** Project administration. **Fafa Nurdyansyah:** Visualization. **Slamet Supriyadi:** Resources. **Dian Marlina:** Investigation. **Retno Ambarwati Sigit Lestari:** Project administration. **Benjamin Walker:** Writing – review & editing, Writing – original draft, Proofread. **Nora Izzati Binti Mohd Razip:** Data curation. **Hironori Kiyooka:** Visualization. **Shota Takemura:** Data curation, Proofread. **Kazuyoshi Ogasawara:** Supervision, Software, Validation.

.

Declaration of competing interest

The authors declare that they have no known competing financial interests or personal relationships that could have appeared to influence the work reported in this paper.

Acknowledgement

We acknowledge the support from Siti Nurfadilah and Retno Setianingsih, students of Magister Pendidikan IPA, Universitas PGRI Semarang. Also Ammar Amjad student of Informatics Department, Faculty of Engineering and Informatics, Universitas PGRI Semarang.

References

[1] J. Buchert, A. Katz, R.R. Alfano, Laser action in emerald, IEEE J. Quant. Electron. 19 (10) (1983).
[2] S.T. Lai, Highly efficient emerald laser, J. Opt. Soc. Am. B 4 (8) (1987).
[3] Z.Q. Chen, G. Zhang, Z. Li, Free running emerald laser pumped by laser diode, Zhongguo Jiguang/Chinese J. Lasers 34 (2) (2007).
[4] V. Antsiferov, Free-running emerald laser, Tech. Phys. 45 (8) (2000) 1085–1087.
[5] T.H. Maiman, Optical and microwave-optical experiments in ruby, Phys. Rev. Lett. 4 (11) (1960) 564–566.
[6] W.M. Fairbank, G.K. Klauminzer, A.L. Schawlow, Excited-state absorption in ruby, emerald, and MgO: Cr3+, Phys. Rev. B 11 (1) (1975) 60–76.
[7] M. Atanasov, E.L. Andreici Eftimie, N.M. Avram, M.G. Brik, F. Neese, First-principles study of optical absorption energies, ligand field and spin-Hamiltonian parameters of Cr3+Ions in emeralds, Inorg. Chem. 61 (1) (2022).
[8] Q. Wei, L.X. Guo, Z.Y. Yang, B. Wei, Studies of the g factors of the ground 4A 2 and the first excited 2E state of Cr 3+ ions in emerald, Spectrochim. Acta Part A Mol. Biomol. Spectrosc. 79 (5) (2011).
[9] Y. Mei, R.M. Peng, W.C. Zheng, Unified research of the optical and EPR spectral data for the trigonal Cr3+ centers in emerald crystals, Optik 127 (8) (2016).
[10] A. Yin, et al., Effects of spin doublets on the ground-state energy levels and Jahn-Teller effects in emerald crystal, Guangzi Xuebao/Acta Photonica Sin. 35 (12) (2006).
[11] H. Wang, X.Y. Kuang, A.J. Mao, Theoretical study of local polarization phenomena of (CrO6)9- cluster in emerald, Wuli Xuebao/Acta Phys. Sin. 59 (5) (2010).
[12] D.W. Yang, M.G. Brik, A.M. Srivastava, C.G. Ma, M. Piasecki, Influence of low-symmetry component of crystal field on gemstones colors: Cr3+ in ruby and emerald, J. Lumin. 221 (2020).
[13] L.E. Orgel, Spectra of transition-metal complexes, J. Chem. Phys. 23 (6) (1955) 1004–1016.
[14] M. Novita, K. Ogasawara, Comparative study of absorption spectra of V 2+ , Cr 3+ , and Mn 4+ in α-Al 2 O 3 based on first-principles configuration–interaction calculations, J. Phys. Soc. Jpn. 81 (10) (Oct. 2012), 104709.
[15] M. Novita, K. Ogasawara, Comparative study of multiplet structures of Mn4+ in K2SiF6, K2GeF6, and K2TiF6 based on first-principles configuration–interaction calculations, Jpn. J. Appl. Phys. 51 (2012), 022604.
[16] M. Novita, D. Marlina, K. Ogasawara, K.J. Seok, K.Y. Soo, Study on the optical luminescence properties of Li2Tio3: Mn4+and Cr3+, Chem. Lett. 50 (1) (2021).
[17] M. Novita, H. Yoshida, K. Ogasawara, Investigation of ion dependence of electronic structure for 3d3 ions in Mg2TiO4based on first-principles calculations, ECS Trans. 50 (41) (2012) 9–17.
[18] M. Novita, K. Ogasawara, Study on multiplet energies of V 2+ , Cr 3+ , and Mn 4+ in MgO host crystal based on first-principles calculations with consideration of lattice relaxation, J. Phys. Soc. Jpn. 83 (12) (2014), 124707.
[19] M. Novita, T. Honma, B. Hong, A. Ohishi, K. Ogasawara, Study of multiplet structures of Mn4+ activated in fluoride crystals, J. Lumin. 169 (2016) 594–600.
[20] M. Novita, H. Nagoshi, A. Sudo, K. Ogasawara, Ab-initio study on the absorption spectrum of color change sapphire based on first-principles calculations with considering lattice relaxation-effect, in: IOP Conference Series: Materials Science and Engineering, 2018.
[21] M. Novita, S. Wibowo, N.Q. Nada, K. Ogasawara, Comparative study on R-line and U-band energies of ruby estimated from one-electron and many-electron first-principles approaches, in: Journal of Physics, Conference Series, 2019.
[22] M. Novita, D. Nuvitalia, K. Ogasawara, A non-empirical lattice-relaxation estimation of TM3+ doped α-Al2O3, IOP Conf. Ser. Mater. Sci. Eng. 850 (2020), 012029.
[23] M. Novita, D. Marlina, N. Cholifah, K. Ogasawara, Study on the Molecular Orbital Energies of Ruby under Pressure, Opt. Mater. (Amst)., 2020.
[24] M. Novita, D. Marlina, N. Cholifah, K. Ogasawara, Enhance electron-correlation effect on the ruby multiplet energy dependence on pressure, Opt. Mater. 110 (2020), 110520.
[25] M. Novita, N. Cholifah, K. Ogasawara, Lattice relaxation effects on the multiplet energies of ruby under pressure using one-electron calculations lattice relaxation effects on the multiplet energies of ruby under pressure using one-electron calculations, IOP Conf. Ser. Mater. Sci. Eng. 835 (2020), 012010.
[26] M. Novita, D. Nuvitalia, N. Cholifah, K. Ogasawara, Optical properties of Co 3 + doped in α-Al 2 O 3 with considering lattice relaxation effect optical properties of Co 3 + doped in α-Al 2 O 3 with considering lattice relaxation effect, IOP Conf. Ser. Mater. Sci. Eng. 835 (5–10) (2020).
[27] K. Ogasawara, T. Ishii, I. Tanaka, H. Adachi, Calculation of multiplet structures of Cr3+ and V3+ in α-Al2O3 based on a hybrid method of density-functional theory and the configuration interaction, Phys. Rev. B 61 (1) (2000) 143–161.
[28] K. Ogasawara, T. Iwata, Y. Koyama, T. Ishii, I. Tanaka, H. Adachi, Relativistic cluster calculation of ligand-field multiplet effects on cation L2,3 x-ray-absorption edges of SrTiO3, NiO, and CaF2, Phys. Rev. B 64 (11) (Aug. 2001), 115413.
[29] M. Novita, I. Farikhah, D. Marlina, C.G. Ma, B. Walker, K. Ogasawara, First-Principles calculations of the interconfigurational transition energies of 4fn - 4fn-15d of Ln3+ ions in LiYF4 and CaF2, Opt. Mater. 122 (2021).
[30] S. Watanabe, K. Ogasawara, M. Yoshino, T. Nagasaki, First-principles and experimental analysis of fn - F n-1 d1 absorption spectra and multiplet energy levels of Pr3+, Nd3+, and U3+ in LiYF4, Phys. Rev. B Condens. Matter 81 (12) (Mar. 2010), 125128.
[31] S. Takemura, M. Novita, K. Ogasawara, Systematic first-principles calculations of charge transfer transitions with structural optimization systematic first-principles calculations of charge transfer transitions of transition metal ions (Sc 3 + , Ti 3 + , V 3 + , Cr 3 + , Mn 3 + , Fe 3 +) in, IOP Conf. Ser. Mater. Sci. Eng. Pap. 835 (2020), 012005.
[32] S. Takemura, K. Ogasawara, Systematic first-principles calculations of charge transfer transitions of trivalent rare earth ions in CaF2, J. Lumin. 214 (2019).
[33] Y. Ohno, CIE fundamentals for color measurements, in: International Conference on Digital Printing Technologies, 2000.
[34] A.D. Broadbent, A critical review of the development of the CIE1931 RGB color-matching functions, Color Res. Appl. 29 (4) (2004).
[35] M. Novita, et al., Chromaticity coordinates of ruby based on first-principles calculation, Opt. Mater. 121 (2021).
[36] B.W. Lawrence, J. West, The structure of beryl, Be 3 Al 2 Si 6 O 18, Proc. R. Soc. Lond. - Ser. A Contain. Pap. Math. Phys. Character 111 (759) (1926).
[37] G. Mathew, R.V. Karanth, T.K. Gundu Rao, R.S. Deshpande, Colouration in natural beryls: a spectroscopic investigation, J. Geol. Soc. India 56 (3) (2000).
[38] E. Fritsch, G.R. Rossman, An update on color in gems. Part 3: colors caused by band gaps and physical phenomena, Gems Gemol. 24 (2) (1988).
[39] K. Nassau, The origin of color in minerals, Am. Mineral. 63 (1978).
[40] J.C.R. Mittani, S. Watanbe, M. Matsuoka, D.L. Baptista, F.C. Zawislak, Doping by diffusion and implantation of V, Cr, Mn and Fe ions in uncoloured beryl crystals, Nucl. Instrum. Methods Phys. Res. Sect. B Beam Interact. Mater. Atoms 218 (2004) 1–4.
[41] J. Fridrichová, P. Bačík, L. Illášová, J. Štubna, R. Škoda, S. Milovská, Forensic gemmological study of green- -coloured beryl of variable origin, Acta Geol. Slovaca 10 (2) (2018).
[42] L.A. Groat, et al., Crystal chemistry of dark blue aquamarine from the true blue showing, Yukon Territory, Canada," Can. Mineral. 48 (3) (2010).
[43] A. Ittipongse, A. Maneewong, K. Pangza, T. Charoennam, The optical characteristic of electron irradiated beryl by UV-Visible and mid-IR spectroscopic analyses, SNRU J. Sci. Technol. 9 (2017) 568–573.
[44] V. Arivazhagan, F.D. Schmitz, P.E. Vullum, A.T.J. van Helvoort, B. Holst, Atomic resolution imaging of beryl: an investigation of the nano-channel occupation, J. Microsc. 265 (2) (2017).
[45] H.A. Hänni, M.S. Krzemnicki, Caesium-rich morganite from Afghanistan and Madagascar, J. Gemmol. 28 (7) (2003).
[46] J. Fridrichová, P. Bačík, A. Ertl, M. Wildner, J. Dekan, M. Miglierini, Jahn-Teller distortion of Mn3+-occupied octahedra in red beryl from Utah indicated by optical spectroscopy, J. Mol. Struct. 1152 (2018).
[47] K. Momma, F. Izumi, VESTA: a three-dimensional visualization system for electronic and structural analysis, J. Appl. Crystallogr. 41 (3) (2008) 653–658.
[48] E. Gaudry, D. Cabaret, C. Brouder, I. Letard, A. Rogalev, F. Wilhlem, N. Jaouen, P. Sainctavit, Relaxations around the substitutional chromium site in emerald: X-ray absorption experiments and density functional calculations, Phys. Rev. B Condens. Matter 76 (9) (2007) 1–10.
[49] R.D. Shannon, C.T. Prewitt, Effective ionic radii in oxides and fluorides, Acta Crystallogr. B 25 (1969) 925–946.
[50] R.D. Shannon, M. H, N.H. Baur, O.H. Gibbs, M. Eu, V. Cu, Revised effective ionic radii and systematic studies of interatomie distances in halides and chaleogenides central research and development department , experimental station , E . L Du pont de Nemours the effective ionic radii of shannon & prewitt, Acta," Acta Cryst. 32 (1976) 751–767.
[51] H. Adachi, M. Tsukada, C. Satoko, Discrete variational Xα cluster calculations. I. Application to metal clusters, J. Phys. Soc. Jpn. 45 (3) (1978) 875–883.
[52] J.C. Slater, J.C. Phillips, Quantum theory of molecules and solids vol. 4: the self-consistent field for molecules and solids, Phys. Today 27 (12) (1974).

[53] C. Satoko, M. Tsukada, H. Adachi, Discrete variational Xa cluster calculations I. Application to the surface electronic structure of MgO, J. Phys. Soc. Jpn. 45 (4) (1978) 1333–1340.
[54] D. Ellis, G. Painter, Discrete variational method for the energy-band problem with general crystal potentials, Phys. Rev. B 2 (8) (1970) 2887.
[55] R.D. Cowan, The Theory of Atomic Structure and Spectra, 1981.
[56] M.N. Taran, K. Langer, A.N. Platonov, V. Indutny, Optical absorption investigation of Cr3+ ion-bearing minerals in the temperature range 77–797 K, Phys. Chem. Miner. 21 (6) (1994).
[57] T.F. Veremeichik, Similarity of ground- and excited-state absorption spectra of Cr3 + ions in a strong crystal field, Phys. Status Solidi 124 (2) (1984).
[58] J. Frguson, D.L. Wood, K. Knox, Crystal-field spectra of d3, d7 ions. II. KCoF 3, CoCl2, CoBr2, and CoWO4, J. Chem. Phys. 39 (4) (1963).
[59] D.L. Wood, Absorption, fluorescence, and zeeman effect in emerald, J. Chem. Phys. 42 (10) (1965).
[60] D.L. Wood, Erratum: absorption, fluorescence, and zeeman effect in emerald [J. Chem. Phys. (1965) 42, (3404)], J. Chem. Phys. 44 (5) (1966).
[61] S. Sugano, Y. Tanabe, H. Kamimura, Multiplets of Transition- Metal Ions in Crystals, Academic Press, New York, 1970.
[62] V. Skvortsova, N. Mironova-Ulmane, L. Trinkler, V. Merkulov, Optical properties of natural and synthetic beryl crystals, IOP Conf. Ser. Mater. Sci. Eng. 77 (2015) 1.
[63] H.H. Kusuma, B. Astuti, Z. Ibrahim, Absorption and emission properties of ruby (Cr:Al2O3) single crystal, J. Phys. Conf. 1170 (1) (2019).
[64] P.K. Tawalare, V.B. Bhatkar, S.K. Omanwar, S.V. Moharil, Cr3+ sensitized near infrared emission in Al2O3:Cr,Nd/Yb phosphors, J. Alloys Compd. 790 (2019).

ld_on_CIE_color_space_based_on_first-principles_calculations.pdf

ORIGINALITY REPORT

24%	20%	18%	6%
SIMILARITY INDEX	INTERNET SOURCES	PUBLICATIONS	STUDENT PAPERS

MATCH ALL SOURCES (ONLY SELECTED SOURCE PRINTED)

1%

★ uis.brage.unit.no

Internet Source

Exclude quotes	Off	Exclude matches	Off
Exclude bibliography	Off		